Analysis and Design of a Low-Cost Well-Performance and Easy-to-Design Current Sensing Circuit Suitable for SiC MOSFETs

Chengzi Yang, *Student Member, IEEE*, Yunqing Pei, *Member, IEEE*, Laili Wang, *Senior Member, IEEE*, Longyang Yu, *Student Member, IEEE*, Cheng Zhao, *Student Member, IEEE*, Mengyu Zhu, and Xingshuo Liu

***Abstract*—Current sense resistor (CSR) is widely used due to cost and integration considerations in industrial applications. However, when CSRs are used to sense transient currents caused by power device switching, especially fast-switching silicon carbide (SiC) metal-oxide-semiconductor field-effect transistors (MOSFETs) with high *di/dt*, even a tiny parasitic inductance in CSRs bring a significant impact on its sensing performance. This article proposes a low-cost well-performance and easy-to-design current sensing circuit that uses the CSRs and an LR compensation network (LRCN) to compensate for the effect of parasitic inductance on transient current sensing. In order to support the parameter selection of the LR network, the effects of parameters such as parasitic capacitance, parasitic inductance, and loads on the performance of the proposed current sensing circuit are analyzed in detail. Meanwhile, a parasitic inductance measurement method that only needs passive probes is proposed to measure and calculate the parasitic inductance of CSRs. This circuit can not only sense the transient current on the printed circuit board level but also observe the transient current on the oscilloscope through a coaxial cable connection. Finally, experimental studies under an inductive load double pulse test setup with SiC MOSFETs are carried out to verify the validity and feasibility of the proposed transient current sensing circuit. Only a high self-resonant frequency inductor and a surface mounted device resistor are needed to form the LR network to fully compensate the effect of parasitic inductance on CSRs.**

***Index Terms*—Current sense resistor (CSR), double pulse test (DPT), parasitic inductance, silicon carbide (SiC) metal-oxide-semiconductor field-effect transistor (MOSFET), transient current sensing.**

NOMENCLATURE

CSRs	Current sensing resistors.
CSB	Current sensing board.
DPT	Double pulse test.
LRCN	LR compensation network.
MOSFETs	Metal-oxide-semiconductor field-effect transistors.
SMD	Surface-mounted device.
SRF	Self-resonant frequency.
SiC	Silicon carbide.
$L_{\rm pe}$	External parasitic inductance of CSR.
$L_{\rm Si}$	Internal parasitic inductance of CSR.
L_S	Total parasitic inductance of CSR.
L_1, L_2, L_3, and L_4	Lead parasitic inductances.
L_C	Compensation inductor.
$L_{\rm Rc}$	Parasitic resistor of $R_{\rm C.}$
$L_{\rm loop}$	Power loop parasitic inductance.
$L_{\rm load}$	Load inductance.
R_S	Resistance of CSR.
R_1, R_2, R_3, and R_4	Lead parasitic resistances.
R_C	Compensation resistor.
R_L	Load input resistor.
$R_{\rm OS}$	Input resistor of oscillator.
R_g	Driver resistor.
C_C	Parasitic capacitor of L_C.
C_L	Load input capacitor.
$C_{\rm in}$	Input capacitor.
$v_{\rm S}$	Voltage sensed on CSR.
$v_{\rm LS}$	Voltage induced on $L_{\rm S}$.
$v_{\rm RS}$	Voltage induced on $R_{\rm S}$.
$v_{\rm SC}$	Output voltage of the proposed current sensing circuit.
$v_{\rm DS}$	Drain-source voltage.
$V_{\rm in}$	Input voltage of DPT.
$\triangle V_{\rm DS}$	Peak to peak values of $v_{\rm DS}$.
$\triangle V_S$	Peak to peak values of $v_{\rm S}$.
$i_{\rm d}$	Measured current/drain current
$G_{\rm sc1}$(s), $G_{\rm sc2}$(s), $G_{\rm sc3}$(s), and $G_{\rm sc4}$(s)	Transfer function models.
$t_{\rm rise}$	Rise time.
$T_{\rm ring}$	Ring period of the drain-source voltage.
$C_{\rm oss@Vin}$	Output capacitance of Q_2 at input voltage $V_{\rm in}$.
Q_1 and Q_2	Tested SiC MOSFETs in DPT.
$\rm BW_{signal}$	Signal bandwidth.
$\rm BW_{probe}$	Bandwidth of measurement devices.

Manuscript received January 16, 2020; revised March 27, 2020; accepted April 22, 2020. Date of publication May 6, 2020; date of current version July 31, 2020. This work was supported in part by the Natural Science Foundation of China under Grant U1966212 and in part by the National Key Research and Development Program of China under Grant 2018YFB0905801. Recommended for publication by Associate Editor D. G. Lamar. *(Corresponding authors: Laili Wang and Yunqing Pei.)*

The authors are with the State Key Laboratory of Electrical Insulation and Power Equipment, Xi'an Jiaotong University, Xi'an 710049, China (e-mail: lemonyang@stu.xjtu.edu.cn; peiyq@mail.xjtu.edu.cn; llwang@mail.xjtu.edu.cn; 382856693@qq.com; zhaocheng3117@stu.xjtu.edu.cn; zmy3118104006@stu.xjtu.edu.cn; liuxingshuo@stu.xjtu.edu.cn).

Color versions of one or more of the figures in this article are available online at https://ieeexplore.ieee.org.

Digital Object Identifier 10.1109/TPEL.2020.2993033

I. Introduction

THE method of sensing and viewing currents using current sense resistors (CSRs) is low-cost, easy-to-design, and high-integration, while providing reasonable accuracy [1] compared with other current sensing method, such as Rogowski coils [2]–[5] and active current transformers [6]. However, CSRs cannot be used to sense transient currents, such as currents caused by power devices switching, especially fast-switching silicon carbide (SiC) metal-oxide-semiconductor field-effect transistors (MOSFETs) [7]–[10], due to the parasitic inductance in CSRs has significant impacts on the sensing performance.

Fig. 1(a) shows the schematic diagram of the double pulse test (DPT) with CSR. Fig. 1(b) presents the parasitic inductance of CSR. Where L_{Pe} is the external parasitic inductance that is mainly cause by the printed circuit board (PCB) layout and can be minimized by advanced layout. L_{Si} is the internal parasitic inductance of CSR, which is mainly determined by the material and manufacturing process and varies greatly between different CSRs. The sum of L_{Pe} and L_{Si} is L_S, the total parasitic inductance of CSR. According to the CSR equivalent circuit shown in Fig. 1(c), the sensing voltage v_S can be expressed as

$$v_S = v_{\mathrm{LS}} + v_{\mathrm{RS}} = L_S \frac{\mathrm{d}i_{\mathrm{D}}}{\mathrm{dt}} + i_D R_S. \tag{1}$$

Even if L_S is as small as 100 pH, the v_{LS} sensing error can reach 100–600 mV when sensing the fast-switching SiC MOSFETs with 1–6 A/ns *di/dt* [7], [8]. At the same time, CSRs are characterized by low values, which normally 0.1–10 mΩ [11] to minimize the power consumption when used in high-power applications. Therefore, the sensing error caused by L_S will greatly affect the sensing accuracy and CSRs cannot directly sense the transient current. Fig. 2 shows the typical waveforms when using CSRs to sense the current during turn-ON and turn-OFF transient.

In order to mitigate the parasitic inductance effects on high-power and high-speed current sensing, coaxial current shunt resistors [12]–[15] and four-terminal Kelvin current sensing resistors [16] were studied.

Using the coaxial current shunt resistor is a high-performance method for sensing transient currents. T&M Research Products Inc. claims that the equivalent bandwidth of coaxial current shunt resistors they produce can be up to 2000 MHz [15]. As shown in Fig. 3(a), the coaxial current shunt resistors utilize its coaxial construction to create a no magnetic field inside [12]. When current flows in the coaxial current shunt resistor through the inner and outer resistance tubes, no significant level of magnetic flux is produced in the inner cylinder [17]. Therefore, the output wires can be extended in this region for the current measurement without any induced voltage due to the high *di/dt*. The equivalent model of the coaxial current shunt resistor is shown in Fig. 3(b) [13]. L_1 and L_2 are parasitic inductances induced by the coaxial current shunt resistors, only a few nH, and have few effects on the high bandwidth measurements. However, due to the coaxial structure and manufacture craft, coaxial current shunt resistors are expensive and large in volume.

The four-terminal Kelvin connection is used to reduce the effect of lead resistance and inductance of high-precision resistors with very low ohmic values in current sensing. The structure and

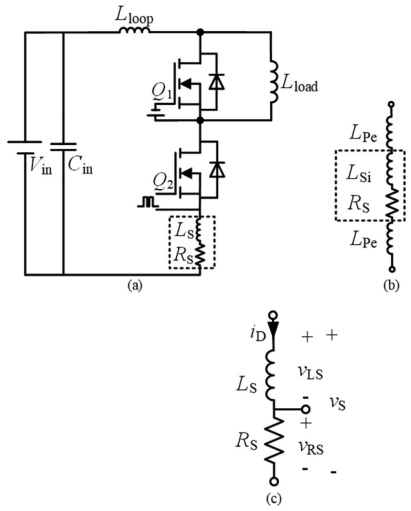

Fig. 1. (a) Schematic diagram of DPT. (b) Parasitic inductance of CSR. (c) Equivalent circuit of CSR.

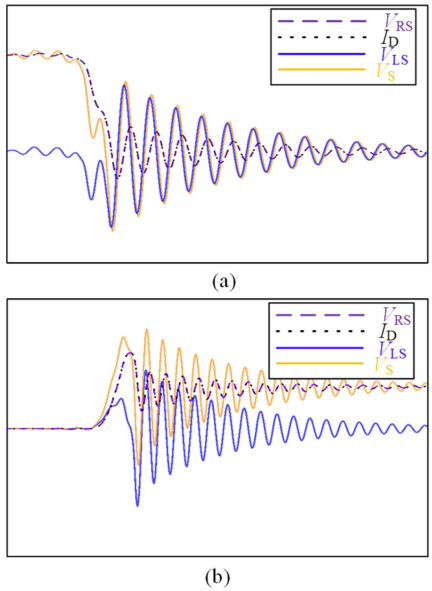

Fig. 2. Typical waveform. (a) Turn-OFF process. (b) Turn-ON process.

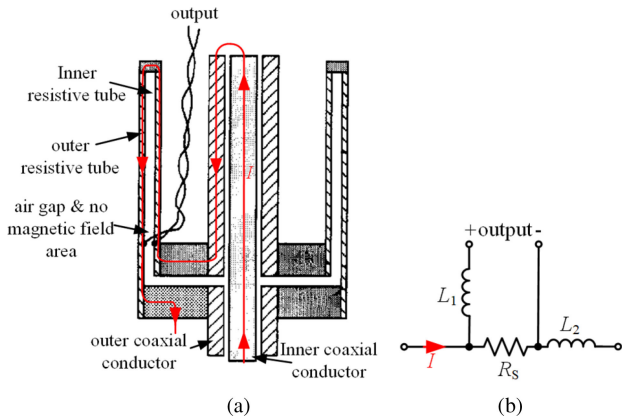

Fig. 3. Coaxial shunt. (a) Internal structure. (b) Equivalent model.

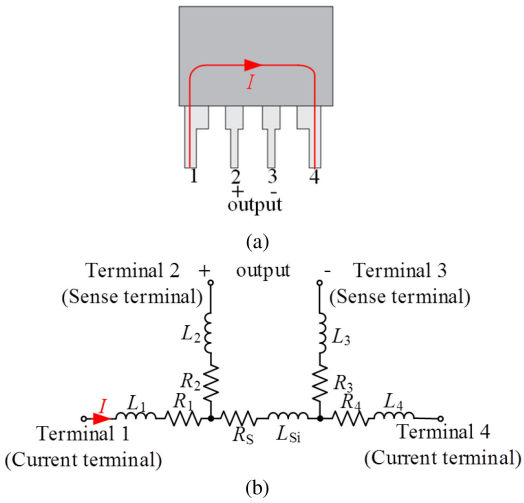

Fig. 4. Four-terminal Kelvin current sensing resistor. (a) Structure. (b) Equivalent model.

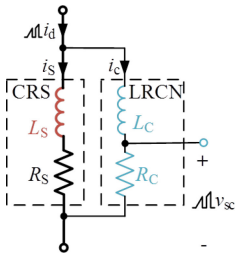

Fig. 5. Proposed high bandwidth current sensing circuit.

equivalent model of the four-terminal Kelvin current resistor are shown in Fig. 4, and the current is forced to flow from terminal 1 to 4. So that the unknown resistances (R_1 and R_4) and inductances (L_1 and L_4) caused by leads attached to terminals 1 and 4 do not affect the performance of the current sensing. And the unknown resistances (R_2 and R_3) and inductances (L_2 and L_3) caused by leads attached to terminals 2 and 3 have essentially zero effect on the output signal because a very high input impedance loads are connected [18]. Although the use of a four-terminal Kelvin connection can avoid the influence of external parasitic inductance on the current sensing, but the influence caused by the internal parasitic inductance L_{Si} cannot be ignored.

In [19], ten 1-Ω 0201 resistors are connected in parallel to measure the fast switching current of GaN devices. By doing so, the equivalent L_{Si} is significantly reduced, but the equivalent L_{Pe} still exists due to the more complex PCB layout than using a single CSR. At the same time, the equivalent resistance and estimated total parasitic inductance are 0.1 Ω and 75 pH, respectively, whose value cannot be used in high-power conditions.

In this article, a current sensing circuit using the LR compensation network (LRCN) to compensate the effect of L_S on CSR's current sensing performance is proposed and analyzed and is shown in Fig. 5. The major advancements of the proposed method are summarized as follows.

1) Only a high self-resonant frequency (SRF) inductor and a surface-mounted device (SMD) resistor are needed to form the LRCN, which presents the advantages of simple-structure, high-integration, and low-cost.
2) The proposed current sensing circuit can not only sense the transient current on the PCB level but also observe the transient current on the oscilloscope through the connection of the coaxial cable.
3) The circuit can be flexibly designed according to the application requirements. At the same time, the parameter selection is easy and the design process is not complicated.

The rest of this article is organized as follows. The basic operation principles and the effects of parameters such as parasitic capacitance, parasitic inductance, and loads on the performance of the proposed current sensing circuit are analyzed in Section II, which provide the theoretical basis for parameter selection. In Section III, a parasitic inductance measurement method that only needs passive probes is proposed to help the parameter design. The proposed current sensing circuit is evaluated by experimental results in Section V. Finally, Section VI concludes this article.

II. Current Sensing and Measurement

A. Basic Operation Principle of the Proposed Current Sensing Circuit

The proposed current sensing circuit consists of a CSR and two passive components that include an SMD resistor and an SMD inductor to form LRCN. As shown in Fig. 5, R_s is the CSR, which has a small resistance value of several milliohms or tens of milliohms to reduce measurement losses. R_c and L_c form LRCN to compensate for the effects of parasitic inductance on high bandwidth current sensing. The output of this high bandwidth current sensing circuit is the voltage v_{sc} on R_C. According to the proposed current sensing circuit shown in Fig. 5, the transfer function model $G_{sc0}(s)$ from i_d to v_{sc} can be expressed as

$$G_{sc0}(s) = \frac{v_{sc}}{i_d} = \frac{R_C \cdot i_c}{i_d} = \frac{R_C}{i_d}\left(i_d \frac{\frac{Z_S \cdot Z_C}{Z_S + Z_C}}{Z_C}\right) = \frac{Z_S \cdot R_C}{Z_S + Z_C} \tag{2}$$

where $Z_S = sL_S + R_S$ and $Z_C = sL_C + R_C$. Thus, $G_{sc0}(s)$ can be expressed as

$$G_{sc0}(s) = \frac{sL_S R_C + R_S R_C}{s(L_S + L_C) + (R_S + R_C)}. \tag{3}$$

If $L_C >> L_S$ and $R_C >> R_S$, $G_{sc0}(s)$ can be further simplified as

$$G_{sc0}(s) = R_S \frac{s^{L_S}/_{R_S} + 1}{s^{L_C}/_{R_C} + 1}. \tag{4}$$

When $L_C/R_C = L_S/R_S$ is satisfied, $G_{sc0}(s)$ can be expressed as

$$G_{sc0}(s) = R_S. \tag{5}$$

From (5), $G_{sc0}(s)$ is frequency independent and is associated with R_S as a constant value when the current sensing circuit meets certain conditions that are $L_C >> L_S$, $R_C >> R_S$, and $L_C/R_C = L_S/R_S$. It should be noticed that due to $L_C >> L_S$ and $R_C >> R_S$ are satisfied, the current flowing through the LRCN

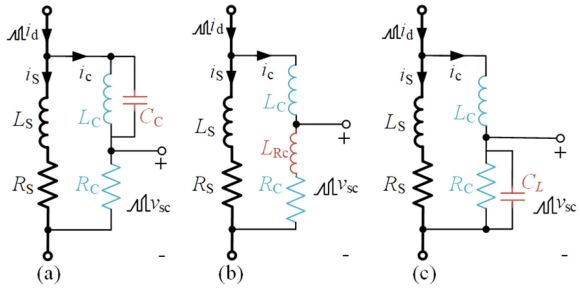

Fig. 6. Current sense circuit considering different parasitic parameters. (a) Parasitic capacitance of L_C. (b) Parasitic inductance of R_C. (c) Load capacitance.

TABLE I
PARAMETERS USED IN SECTION II

Components	Descriptions
R_S	0.01 Ω
L_S	0.5 nH
L_C	100 nH to 10 μH
R_C	2 Ω to 200Ω*
C_C	0.5 pF to 2.5 pF**
L_{Rc}	1 nH to 5 nH**
C_L	1 pF to 9 pF**

*The value of R_C depends on the value of L_C that satisfies $L_C/R_C = L_S/R_S$.
**These parameters are divided into five equal parts within this range.

is very small. Therefore, the resistor and inductor that form the LRCN only need components with small packages.

B. Parasitic Parameters Effects on the Performance of the Proposed Current Sensing Circuit

1) C_C: Parasitic Capacitor of L_C: According to the current sensing circuit considering the parasitic capacitor of L_C shown in Fig. 6(a), the transfer function model $G_{sc1}(s)$ from i_d to v_{sc} considering C_C the parasitic capacitor of L_C can be expressed as

$$G_{sc1}(s) = \frac{v_{sc}}{i_d} = \frac{Z_S \cdot R_C}{Z_S + Z_C} \tag{6}$$

where $Z_S = sL_S + R_S$ and $Z_C = \frac{sL_C}{s^2C_CL_C+1} + R_C$. Thus, $G_{sc1}(s)$ can be expressed as

$$G_{sc1}(s) = \frac{(sL_S + wR_S)(s^2C_CL_C + 1)R_C}{(sL_S + R_S)(s^2C_CL_C + 1) + s^2C_CL_CR_C + sL_C + R_C}. \tag{7}$$

If $L_C>>L_S$, $R_C>>R_S$ are satisfied, $G_{sc1}(s)$ can be further simplified as

$$G_{sc1}(s) = R_S\frac{\left(s\frac{L_S}{R_S}+1\right)\left(s^2C_CL_C+1\right)}{\left(s\frac{L_C}{R_C}+1\right)+s^2C_CL_C}. \tag{8}$$

According to (8) and the parameters listed in Table I, considering the influence of C_C, the characteristics of the proposed

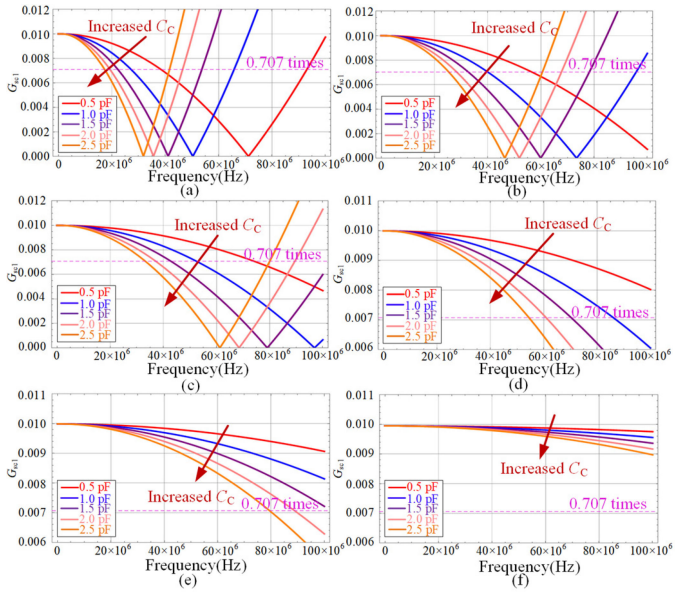

Fig. 7. Calculated characteristics of proposed current sensing circuit affected by C_C from 0.5 to 2.5 pF. The inductance of L_C: (a) 10 μH, (b) 4.7 μH, (c) 2.7 μH, (d) 1 μH, (e) 470 nH, and (f) 100 nH.

current sensing circuit in the frequency domain can be calculated and depicted in Fig. 7. The effects of C_C from 0.5 to 2.5 pF on the current sensing circuit are show in Fig. 7 when the values of L_C are 10 μH, 4.7 μH, 2.7 μH, 1 μH, 470 nH, and 100 nH, respectively. The magnitude of G_{sc1} under low-frequency conditions is 0.01, which is the value of R_S. But as the frequency increases, the magnitudes of G_{sc1} decays, and the larger is C_C, the faster the signal decays. For Fig. 7(a)–(c), the magnitudes of G_{sc1} have corner frequencies within the range of 100 MHz. As the value of C_C decreases, the corner frequency increases. For Fig. 7(d)–(f), the corner frequency can be higher than 100 MHz. As the value of L_C decrease, the decay rate of magnitudes of G_{sc1} decreases, thus the current sensing circuit can obtain a higher bandwidth. In conclusion, when only considering the effects of C_C, the values of L_C and C_C should be as small as possible to achieve higher bandwidth.

2) L_{RC}: Parasitic Inductor of R_C: According to the current sensing circuit considering L_{RC} the parasitic inductance of R_C shown in Fig. 6(b), the transfer function model $G_{sc2}(s)$ from i_d to v_{sc} considering L_{RC} can be expressed as

$$G_{sc2}(s) = \frac{v_{sc}}{i_d} = \frac{Z_S\left(R_C + sL_{RC}\right)}{Z_S + Z_C} \tag{9}$$

where $Z_S = sL_S + R_S$ and $Z_C = s(L_C + L_{RC}) + R_C$. Thus, $G_{sc2}(s)$ can be expressed as

$$G_{sc2}(s) = \frac{s^2L_{RC}L_S + s\left(R_CL_S + L_{RC}R_S\right) + R_CR_S}{s\left(L_S + L_C + L_{RC}\right) + R_C + R_S}. \tag{10}$$

If $L_C>>L_S$, $R_C>>R_S$ are satisfied, $G_{sc2}(s)$ can be further simplified as

$$G_{sc2}(s) = R_S\frac{\left(s\frac{L_S}{R_S}+1\right)+s^2\frac{L_{RC}L_S}{R_CR_S}+s\frac{L_{RC}}{R_C}}{\left(s\frac{L_C+L_{RC}}{R_C}+1\right)}. \tag{11}$$

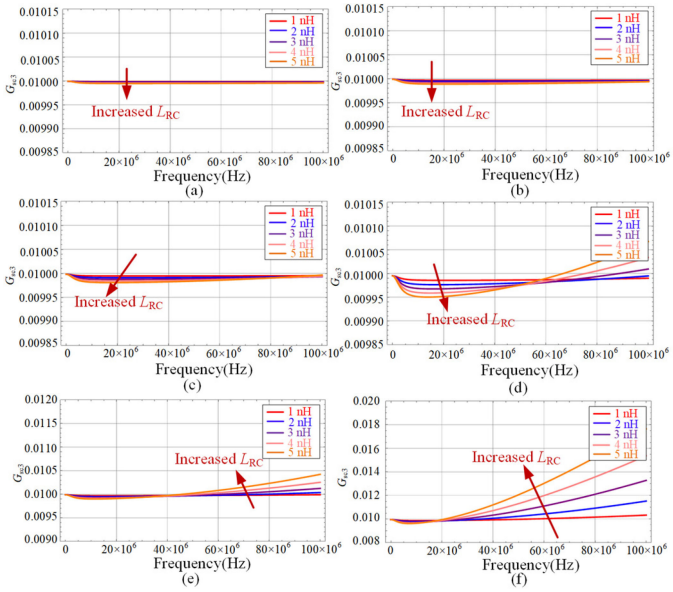

Fig. 8. Calculated characteristics of proposed current sensing circuit affected by L_{RC} from 1 to 5 nH. The value of L_C: (a) 10 μH, (b) 4.7 μH, (c) 2.7 μH, (d) 1 μH, (e) 470 nH, and (f) 100 nH.

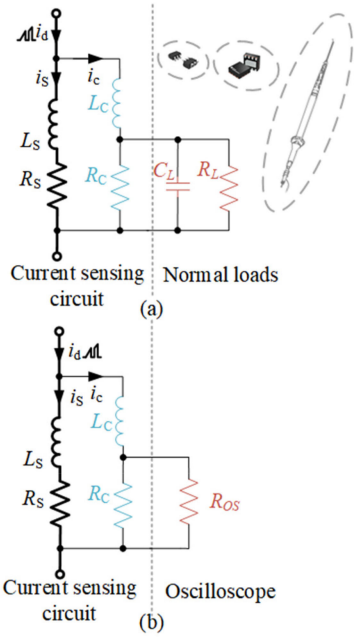

Fig. 9. Schematic diagram of the sensing circuit with different loads. (a) Normal loads. (b) Oscilloscope.

According to (11) and the parameters listed in Table I, considering the influence of L_{RC}, characteristics of the proposed current sensing circuit in the frequency domain can be calculated, as depicted in Fig. 8. The influence on the parasitic resistance L_{RC} from 1 to 5 nH are shown in Fig. 8 when the values of L_C are 10 μH, 4.7 μH, 2.7 μH, 1 μH, 470 nH, and 100 nH, respectively. As shown in Fig. 8(a)–(c), when the value of L_C is larger than 2.7 μH, the change of L_{RC} has almost no effect on G_{sc2}. When the value of L_C is within the range of 1 μH to 470 nH, the change of the value of L_{RC} has acceptable effects on G_{sc2}, which is shown in Fig. 8(d) and (e). In these conditions, the worst-case error is less than 5%, therefore the effect can be neglected. As depicted in Fig. 8(f), when the value of L_C is 100 nH, the effect on the magnitudes of G_{sc2} becomes significant as L_{RC} increases. In summary, when the value of L_C is large than 470 nH, the effect of L_{RC} on the magnitudes of G_{sc2} can be neglected.

3) Load Effect: The loads analysis can be divided into two cases, one is with the normal load, and the other is that the output signal of the proposed current sensing circuit v_{sc} is sent directly to the oscilloscope. The schematic diagrams of these two conditions are illustrated in Fig. 9.

In Fig. 9(a), a normal load such as a high-speed operational amplifier, a high-speed comparator, a high-speed ADC chip, and a voltage probe has several pF input capacitance C_L and several MΩ input resistance R_L. At this condition, R_L is thousands of times larger than R_C, thus the effect of R_L on R_C can be ignored. Therefore, only C_L is considered here.

According to the current sensing circuit considering C_L shown in Fig. 6(c), the transfer function model $G_{sc3}(s)$ from i_d to v_{sc} considering the load capacitor can be expressed as

$$G_{sc3}(s) = \frac{v_{sc}}{i_d} = \frac{R_C}{sR_CC_L + 1} \cdot \frac{Z_S}{Z_S + Z_C} \tag{12}$$

where $Z_S = sL_S + R_S$ and $Z_C = sL_C + R_C/(sR_CC_L + 1)$. Thus, $G_{sc3}(s)$ can be expressed as

$$G_{sc3}(s) = \frac{(sL_S + R_S)\,R_C}{(s\,(L_S + L_C) + R_S)\,(sR_CC_L + 1) + R_C}. \tag{13}$$

If $L_C >> L_S$, $R_C >> R_S$ are satisfied, $G_{sc3}(s)$ can be further simplified as

$$G_{sc3}(s) = R_S \frac{\left(s\frac{L_S}{R_S} + 1\right)}{\left(s\frac{L_C}{R_C} + \frac{R_S}{R_C}\right)(sR_CC_L + 1) + 1}. \tag{14}$$

According to (14) and the parameters listed in Table I, considering the influence of C_L, the characteristics of the proposed current sensing circuit in the frequency domain can be calculated, as depicted in Fig. 10. The influence on C_L from 1 to 9 pF are shown in Fig. 10 when the values of L_C are 10 μH, 4.7 μH, 2.7 μH, 1 μH, 470 nH, and 100 nH, respectively. The dc magnitude of G_{sc3} is 0.01, which is the value of R_S when the value of L_C is large. However, when the value of L_C is less than 1 μH, the dc magnitude of G_{sc3} is slightly less than 0.01, which is mainly because the value of R_C decreases as the value of L_C decreases to satisfy $L_C/R_C = L_S/R_S$. Under dc conditions, too small R_C affects the magnitude of G_{sc3}. On the other hand, it can be seen from Fig. 10 that when the value of C_L increases, but is within 5 pF, the value of L_C and frequency have an acceptable effect on the magnitude of G_{sc3}. When the value of L_C is less than 2.7 μH, as shown in Fig. 10(c), (d), and (f), further increase in C_L has almost no effect on G_{sc3}. However, when the values of L_C are 10 and 4.7 μH, a further increase in C_L will apparently reduce the magnitudes of G_{sc3}, as depicted in Fig. 10(a) and (b). That is, when the value of L_c is larger than 2.7 μH, C_L should be controlled within 5 pF to obtain a higher bandwidth, when

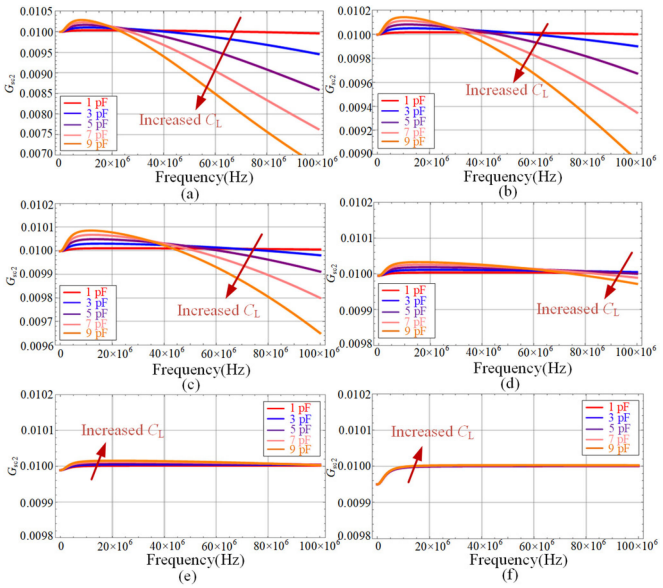

Fig. 10. Calculated characteristics of proposed current sensing circuit affected by C_L from 1 to 9 pF. The value of L_C: (a) 10 μH, (b) 4.7 μH, (b) 2.7 μH, (c) 1 μH, (d) 470 nH, and (f) 100 nH.

the value of L_C is less than 2.7 μH, the effects of C_L on G_{sc3} are weak and can be neglected.

In Fig. 9(b), v_{sc} is directly sent to an oscilloscope with 50 Ω input resistance R_{OS}. At this condition, the constraint of the proposed circuit becomes

$$\frac{L_S}{R_S} = \frac{L_C}{R_{OS}} + \frac{L_C}{R_C}. \tag{15}$$

C. Design Recommendations

As discussed above, to guide the design of high bandwidth current sensing circuit, the following design recommendations can be summarized.

1) The value of L_C should be no more than 4.7 μH to minimize the effect of C_C, and should be larger than 470 nH to minimize the effect of L_{RC}.

2) When the value of L_C is less than 4.7 μH, C_L has no obvious impact on the sensing circuit when using loads such as high-speed operational amplifier, high-speed comparator, high-speed ADC chip, and probes because C_L introduced by them is small and only a few pF. It is not recommended to use other values of L_C. If the value of L_C larger than 4.7μH is selected, the value of C_L should be carefully controlled.

3) The value of C_C has a significant impact on the performance of the sensing circuit. Therefore, the compensation inductor here needs a careful selection. High SRF inductors with SRF above 50 MHz and designed for high-frequency applications are recommended. In this article, a 1-μH compensation inductor with 0805 package and 160-MHz SRF is selected, which means its equivalent parasitic capacitance is about 0.99 pF. According to Fig. 7, in this condition, the designed bandwidth of the proposed current sensing circuit is about 85 MHz.

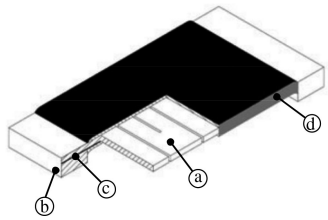

Fig. 11. Clad construction of the SMD CSRs. (a) Resistive element. (b) Terminal. (c) Terminal to element cladding. (d) High-temperature encapsulant.

The signal bandwidth $\mathrm{BW_{signal}}$ is given as follows [20]:

$$\mathrm{BW_{signal}} = \frac{0.35}{t_{\mathrm{rise}}} \tag{16}$$

where t_{rise} is the rise time of a signal, which is the time it takes to rise from 10% to 90% of its final value.

At the same time, to obtain an accurate measurement results, the bandwidth of measurement devices $\mathrm{BW_{probe}}$ should be at least three times higher than the tested signal [20], [21]. That is

$$\mathrm{BW_{probe}} \geq 3\mathrm{BW_{signal}}. \tag{17}$$

Combining (16) and (17), a current sensing circuit with 85-MHz bandwidth can be used to sense signals whose rise time is as fast as 12.3 ns and can satisfy the requirement of most tested SiC MOSFETs [7]–[10], [22], [23]. If a faster transient current is tested, according to Fig. 7, an inductor with higher SRF or a L_C with smaller inductance is recommended.

4) When using CSRs to sense high bandwidth currents, careful considerations should be given to the skin effects. The clad construction of the SMD CSRs is shown in Fig. 11 [24]. The thickness of the resistor element determines the skin effect. To mitigate the skin effect, on the one hand, all welded construction of the power metal strip resistors with 0603 package form Vishay is selected as the CSRs which thickness of resistive element and high temperature encapsulant is only 0.15 mm, while the thickness of the conventional 0603 resistors is more than twice. On the other hand, using multiple CSRs in parallel can further reduce the skin effect. At the same time, there should be gaps in the layout of multiple CSRs to avoid the proximity effect.

5) PCB layout and routing should be carefully designed to avoid electromagnetic interference. R_S, L_C, and R_C should be placed as close as possible. Connecting these three devices directly by wiring will bring a relatively large loop area, as shown in Fig. 12(a). Therefore, as shown in Fig. 12(b), it is recommended to use polygon pour to interconnect *RLC* here, and the output wire should be carefully routed between the two pads of R_C to ensure a minimum loop area. When R_C shares ground with the converter, large ground coverage can effectively reduce loop area, which is shown in Fig. 12(c).

6) When designing the proposed current sensing circuit, CSR should be first designed considering the amplitude of the output voltage and the power loss in different current ratings. Then, design an LRCN for the selected CSR according to the design method and considerations discussed in this Section.

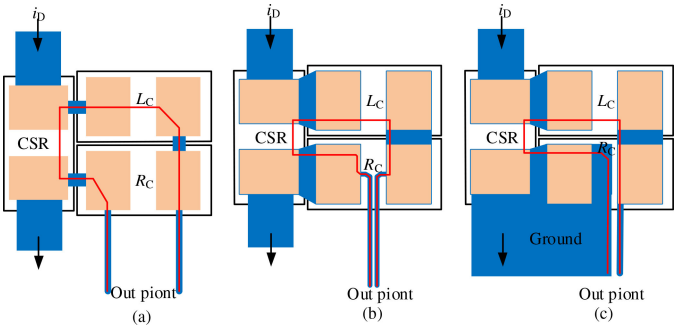

Fig. 12. PCB layout and routing. (a) Normal. (b) Optimized. (c) Optimized when shares ground.

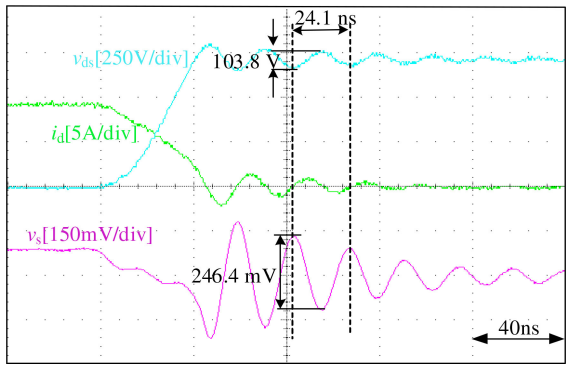

Fig. 13. Experimental results for L_S calculation.

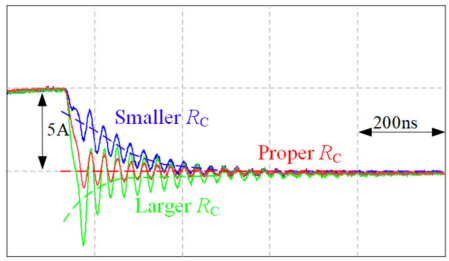

Fig. 14. Test results of the proposed current sensing circuit with different R_C.

III. Experimental Preparation

A. Measurement Method of L_S

Before designing a high-bandwidth current detection circuit, it is necessary to obtain the key parameter L_S through measurement. In this section, a simple and accurate L_S test method is proposed.

In this article, the experimental setup is the inductive load DPT setup, as shown in Fig. 1(a). And the typical turn-OFF switching waveforms of Q_2 are shown in Fig. 12.

The sum of power loop inductance L_{loop} and L_s can be obtained by [25]–[27]

$$L_{\text{loop}} + L_S = \frac{T_{\text{ring}}^2}{4\pi^2 C_{\text{oss@Vin}}} \tag{18}$$

where T_{ring} is the ringing period of the drain-source voltage, which is equal to t_3 minus t_1. $C_{\text{oss@Vin}}$ is the output capacitance of Q_2 at input voltage V_{in}. It should be noticed that V_{in} should be larger enough to avoid the change in C_{oss} caused by the drain-source voltage oscillation of Q_2. In this article, V_{in} is set to 700 V for SiC MOSFET IMW120R045M1 to avoid this error.

As shown in Fig. 1, the voltage that can be directly tested by the probe is v_s, and it can be expressed as

$$v_s = v_{\text{Ls}} + v_{\text{Rs}} = L_S \frac{\text{d}i_{\text{D}}}{\text{dt}} + i_D R_s. \tag{19}$$

It is worth noting that v_s is composed of two parts, one is v_{Ls} which is related to the L_S and di_D/dt and is proportional to the voltage drop on L_{loop}, and the other is v_{Rs} which is not directly proportional to L_{loop}. However, at t_1 and t_2, v_S and v_{DS} reach their positive and negative peak points, i_D is zero at this time according to the LC circuit resonance law. Thus, at t_1 and t_2, v_{Rs} is zero, and we can obtain that

$$\frac{\Delta V_{\text{DS}}}{\Delta V_S} = \frac{L_{\text{loop}} + L_{\text{S}}}{L_{\text{S}}} \tag{20}$$

where $\triangle V_{\text{DS}}$ and $\triangle V_S$ are the peak to peak values of V_{DS} and V_S between t_1 and t_2, respectively.

Combining (18) and (20), we can obtain

$$L_S = \frac{T_{\text{ring}}^2}{4\pi^2 C_{\text{oss@Vin}}} \frac{\Delta V_S}{\Delta V_{\text{DS}}}. \tag{21}$$

From (19), it can be found that only the passive voltage probe is required in the test of L_{S} by using the test method proposed in this section. Experimental waveforms are shown in Fig. 13, L_s can be obtained from the measured data, which is 0.303 nH in our design.

B. Correction

Even though the parameter selection of the proposed current sensing circuit is based on the theoretical analysis discussed above, the correction is also needed due to there are some inevitable errors caused by the measurement deviations and component parameter tolerances.

In Fig. 14, the test results of the proposed current sensing circuit with different R_C are depicted. The signal with a smaller R_C, which is depicted in blue, has a positive oscillating center at first, and the oscillating center gradually drops to zero. In contrast, the signal with a larger R_C, shown in green, has a negative oscillating center until the oscillating center drops to zero. If R_C is a proper value, the oscillation of the test signal will be centered at zero in the first time. It should be noticed that in Fig. 14, the value of R_C is intentionally enlarged or reduced to show the influence of the parameter on the test results. In actual design, it is not much different from the proper R_C and design R_C, and some fine-tuning is enough.

IV. Experimental Verification

A. Experimental Prototype

To validate the performance of the current sensing circuit proposed in this article, a DPT experimental setup with inductive

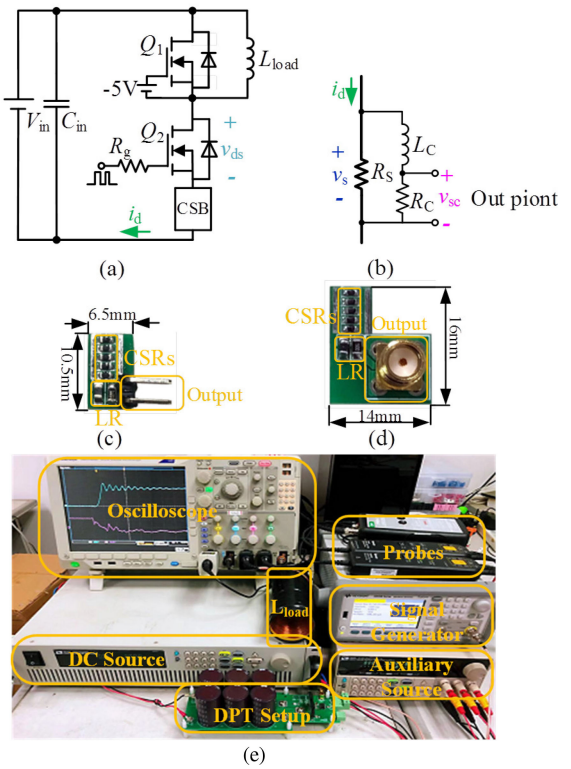

Fig. 15. Experimental test rig. (a) Schematic diagram of DPT. (b) Schematic diagram of CSB. (c) CSB with normal load. (d) CSB with coaxial cable and oscilloscope. (e) Test facilities.

TABLE II
PARAMETERS IN THE EXPERIMENTAL SETUP

Components	Values	Descriptions
Q_1,Q_2	1200 V, 52 A	IMW120R045M1 from Infineon
C_{in}	1.02 mF,900 V	Electrolytic capacitors from Lelon
L_{load}	150 μH	Air core inductor
R_s	0.01 Ω, 2 W	0603 resistors from Vishay
R_g	10 Ω	0805 resistors from Yageo
L_C	1 mH, 160 MHz	KLZ2012MHR1R0HTD25 from TDK
R_C	130 Ω	0805 resistor from Yageo

load is built, of which the schematic diagram is shown in Fig. 15(a). Fig. 15(b) shows the schematic diagram of the current sensing board (CSB). The SiC MOSFETs, IMW120R045M1 from Infineon, are employed as devices under test. The lower SiC MOSFET serves as the device under test and the upper one serves as the freewheeling diode. The oscilloscope is MDO4104C with a bandwidth of 1 GHz. The current probe TCP0020 (100 A/50 MHz) is employed to detect the drain current of SiC MOSFET Q_2, and the results are compared with the proposed current sensing method in this article. The voltage probe THDP0200 (1500 V/200 MHz) is used to measure the drain-source voltage of Q_2. The parameters of the components in the experimental setup are shown in Table II, and Fig. 15(c)–(e) shows the photograph of the established hardware prototype. R_S is 0.01 Ω and 2 W, which is composed of five 0603 50-mΩ CSRs WSLP0603R0500FEB in parallel. A 0805 1-μH inductor L_C and a 0805 130-Ω resistor R_C form the LRCN. It can be found in Fig 15(c) and (d) that the proposed CSB has a small volume as well.

B. Verification by Double Pulse Test Results

In order to verify the performance of the proposed voltage sensing circuit, DPT is carried out with a 10-Ω gate resistor both in turn-ON and turn-OFF. The experimental DPT results with 200-V bus voltage are shown in Fig. 16(a) and the zoom-in views are shown in Fig. 16(b)–(d). Where v_{ds} is the drain-source voltage of Q_2, v_{sc} is the output of the proposed current sensing circuit, i_d is the drain current of SiC MOSFETs $Q2$ and v_s is the voltage of R_S, which shows the influence of parasitic inductance on the current sensing.

Fig. 16(a) shows that v_{sc} matches i_d well, in both the switching stage and ON/OFF stage. However, v_s has a large difference between i_d during the switching stage, but it matches i_d well during ON/OFF stage. This means that the proposed current sensing circuit can well compensate the effect of parasitic inductance on current sensing when using CSRs. The zoom-in views of the first turn-ON process, the first turn-OFF process, and the second turn-ON process further illustrate the conclusion.

C. Verification by Waveform Comparison

In order to further verify the performance of the proposed voltage sensing circuit, turn-ON and turn-OFF processes with different load current i_L are carried out. Fig. 17 shows test results when the load current varies from 5 to 30 A under the same test condition as the DPT. On the one hand, the drain current is close to the load current before Q_2 turns OFF, and its steady-state value reaches zero after the turn-OFF oscillation. The drain current is zero before Q_2 begins to turn ON and reaches the load current after Q_2. On the other hand, the waveforms measured by the current probe and sensed by the proposed method are well matched, expect that the oscillation amplitude sensed by the proposed method is slightly larger than that measured by the current probe. All of these can verify the accuracy and correctness of the proposed method.

V. ANALYSIS AND DISCUSSION

To discuss the performance of the proposed current sensing circuit, the cost, bandwidth, volume, flexibility, difficulty, and isolation of the proposed method and existing methods are discussed in detailed and listed in Table III.

A. Cost

According to Fig. 15 and Table II, five 0603 50-mΩ 0.4-W CSRs WSLP0603R0500FEB with the price $0.32 per unit from Vishay connected in parallel to form the R_S and a 0805 inductor KLZ2012MHR1R0HTD25 L_C with the price $0.3 per unit from TDK and a 0805 resistor *RC* with the price $0.03 per unit from Yageo were used. In addition, the connectors have a very low price and do not count here. Therefore, the total cost of the proposed current sensing circuit with 0.01 Ω 2 W 85 MHz is about $1.93, and it was calculated just for one unit, not for large series. At the same time, a current shunt with 0.01 Ω 2 W from T&M (400 MHz) [28] is about $350 and from Cybertek (120 MHz) [29] is about $240. In addition, the current probe which uses active current transformer technology TCP0020 from Tektronix

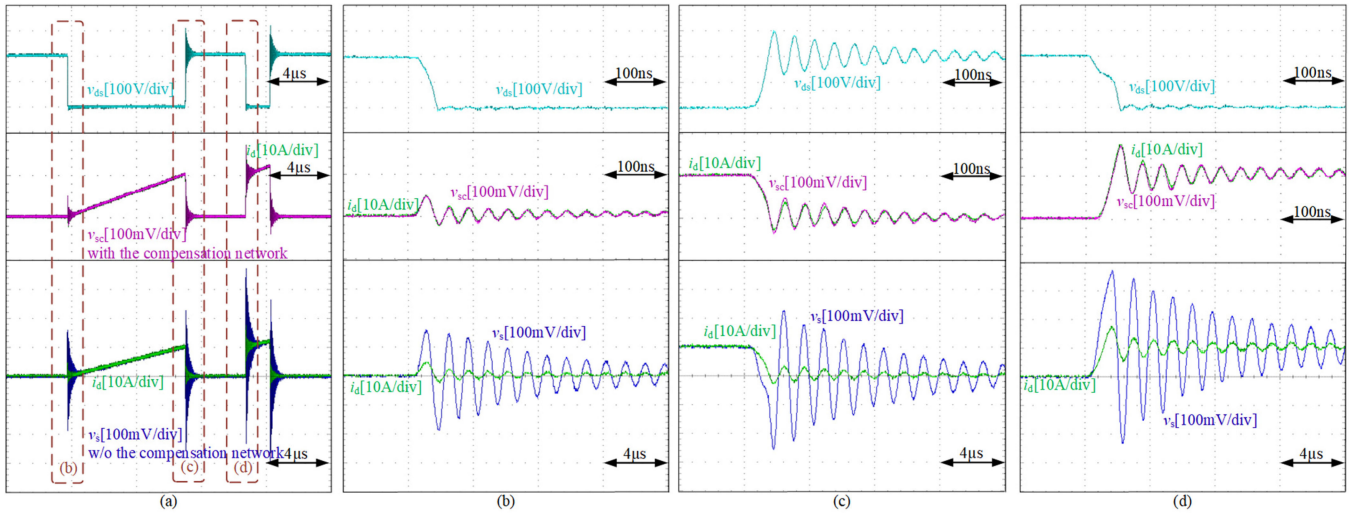

Fig. 16. Experimental results. (a) DPT results. (b) Zoom-in view of the first turn-ON process. (c) Zoom-in view of the first turn-OFF process. (d) Zoom-in view of the second turn-ON process.

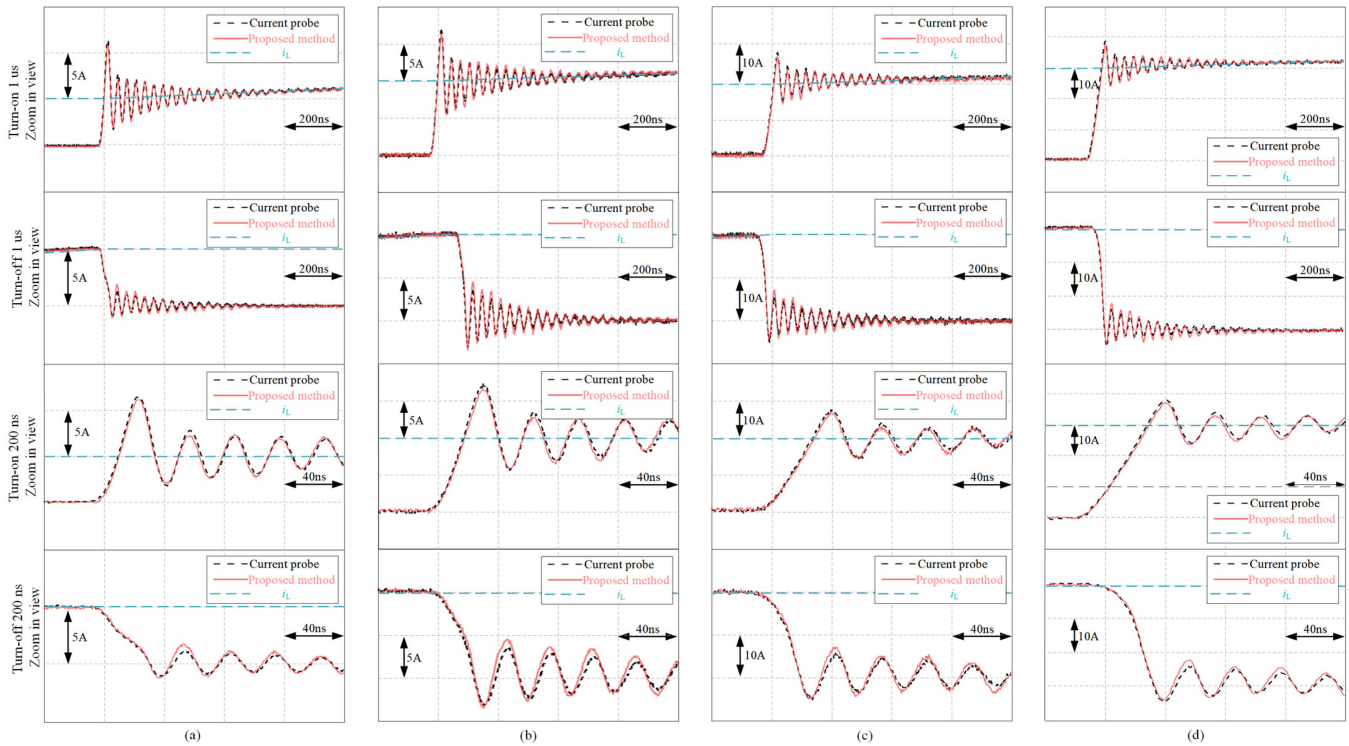

Fig. 17. Drain current waveforms when inductor current changes. (a) 5 A. (b) 10 A. (c) 20 A. (d) 30 A. From top to bootom, turn-ON process.

TABLE III
PERFORMANCE COMPARISON OF CURRENT MEASUREMENTS

Method	COST	Bandwidth	Volume	Flexibility	Difficulty	Isolation
Proposed method	Very low	Medium	Very small	High	Very low	No
Coaxial shunt	Medium	Very high	Large	Medium	High	No
Current probe	High	Medium	Large	Low	High	Yes
Rogowski coil	Medium	Low	Large	Medium	High	Yes

(100A 50 MHz) [30] is about $3600 and a Rogowski coil CWT MiniHF 06 from PEM (120A 30 MHz) [31] is about $1800. Thus, the proposed method has a significant advantage in cost.

B. Bandwidth

According to the analysis in Section II, the bandwidth of the proposed current sensing circuit is mainly determined by the value of the parasitic inductance of L_C. In this article, a 1-μH 160-MHz SRF inductor and the bandwidth of the proposed current sensing circuit is about 85 MHz in the theoretical analysis, which is enough for high-power SiC current measurement. And in Section IV, the full comparisons with 50-MHz current probe from Tektronix prove that the bandwidth of the proposed current sensing circuit is not lower than 50 MHz. If a higher bandwidth of the proposed current sensing circuit is wanted, the L_C with higher SRF is needed. At the same time, coaxial shunts with 0.01 Ω and 2 W have a bandwidth up to 400 MHz and are the current measurement method with the highest bandwidth. Due to the impact of the performance of the integrating circuit, the current probe and Rogowski coil have a limited bandwidth. In addition, the multiple turns structure, which is aimed to increase the sensitivity, will lead to a large coil inductance and parasitic capacitance and further limit the bandwidth [17]. That is, the proposed method has enough bandwidth for high-power SiC current measurement and the bandwidth can be further expand.

C. Volume

According Fig. 15(c) and (d), the proposed current sensing circuit has a very small volume that is suitable for high integration requirements. However, due to the special coaxial structure, the volume of the coaxial shunts will not be small. And the volume of the measurement method by using an active current transformer or Rogowski coil is limited by the active signal process circuits and its auxiliary power supply circuit [1]. Which means, the proposed method has advantages on volume and is a good choice for high integration requirements.

D. Flexibility and Design Difficulty

The proposed method has advantages of flexible to design and high reliable, which inherits from CRSs, and the design process is easy compared with other current measurement methods [1]. What's more, the proposed method not only can be used in current measurement on an oscilloscope, but can also sense the current on boards. This also presents the flexibility of the proposed method compared with coaxial shunts and current probes.

E. Isolation

The proposed method is short, on that, there is no isolation between the measured current and the output signal. And this is the same as coaxial shunts and CSRs. Therefore, when using the proposed method to sense current, attention should be paid to grounding issues.

VI. Conclusion

In this article, a current sensing circuit based on the LR compensation circuit has been presented for the problem that CSRs cannot directly sense transient current. The LRCN that meets certain constraints can well compensate the influence of parasitic inductance in CSRs and accurately detect dynamic current. The proposed current circuit with 0.01 Ω 2 W CRSs and the corresponding compensation network have been tested and compared on SiC MOSFETs based DPT experimental setup. The proposed current sensing circuit has the advantages of low cost, small volume, easy-to-design, and high bandwidth for high-power SiC MOSFET current sensing.

References

[1] S. Ziegler, R. C. Woodward, H. H. C. Iu, and L. J. Bolre, "Current sensing techniques: A review," *IEEE Sens. J.*, vol. 9, no. 4, pp. 354–376, Apr. 2009.

[2] J. Wang, Z. Shen, R. Burgos, and D. Boroyevich, "Design of a high-bandwidth Rogowski current sensor for gate-drive shortcircuit protection of 1.7 kV SiC MOSFET power modules," in *Proc. IEEE Workshop Wide Bandgap Power Dev. Appl.*, 2015, pp. 104–107.

[3] L. Zhao, J. D. v.Wyk, and W. G. Odendaal, "Planar embedded pick-up coil sensor for integrated power electronic modules," in *Proc. Appl. Power Electron. Conf. Expo.* , 2004, vol. 2, pp. 945–951.

[4] Y. Xue, J. Lu, Z. Wang, L. M. Tolbert, B. J. Blalock, and F. Wang, "A compact planar Rogowski coil current sensor for active current balancing of parallel-connected silicon carbide MOSFETs," in *Proc. IEEE Energy Convers. Congr. Expo.*, 2014, pp. 4685–4690.

[5] E. Farjah, H. Givi, and T. Ghanbari, "Application of an efficient rogowski coil sensor for switch fault diagnosis and capacitor ESR monitoring in non-isolated single-switch DC–DC converters," *IEEE Trans. Power Electron.*, vol. 32, no. 2, pp. 1442–1456, Feb. 2017.

[6] P. Poulichet, F. Costa, and É. Labouré, "A new high-current largeband-width DC active current probe for power electronics measurements," *IEEE Trans. Ind. Electron.*, vol. 52, no. 1, pp. 243–254, Feb. 2005.

[7] H. Li, X. Liao, Y. Hu, Z. Zeng, E. Song, and H. Xiao, "Analysis of SiC MOSFET di/dt and its temperature dependence," *IET Power Electron.*, vol. 11, no. 3, pp. 491–500, Mar. 2018.

[8] L. Zhang, X. Yuan, X. Wu, C. Shi, J. Zhang, and Y. Zhang, "Performance evaluation of high-power SiC MOSFET modules in comparison to Si IGBT modules," *IEEE Trans. Power Electron.*, vol. 34, no. 2, pp. 1181–1196, Feb. 2019.

[9] Z. Chen, *et al.*, "Development of a 1200 V, 120 A SiC MOSFET module for high-temperature and high-frequency applications," in *Proc. IEEE Workshop Wide Bandgap Power Devices Appl.*, Oct. 2013, pp. 52–59.

[10] S. Hazra *et al.*, "High switching performance of 1700v, 50A SiC power MOSFET over Si IGBT/BiMOSFET for advanced power conversion applications," *IEEE Trans. Power Electron.*, vol. 31, no. 7, pp. 4742–4754, Jul. 2015.

[11] TOKEN ELECTRONICS, Low Ohm Chip, 2009. [Online]. Available: http://www.token.com.tw/.

[12] C. M. Johnson and P. R. Palmer, "Current measurement using compensated coaxial shunts," *IEE Proc.—Sci., Meas. Technol.*, vol. 141, no. 6, pp. 471–480, Nov. 1994.

[13] Z. Chen, "Characterization and modeling of high-switching-speed behavior of SiC active devices," M.S. thesis, Dept. of Elect. Eng., Virginia Tech, Blacksburg, VA, USA, 2009.

[14] Z. Liu, X. Huang, F. C. Lee, and Q. Li, "Package parasitic inductance extraction and simulation model development for the high-voltage cascode GaN HEMT," *IEEE Trans. Power Electron.*, vol. 29, no. 4, pp. 1977–1985, Apr. 2014.

[15] T&M Research Products, Inc., Current Viewing Resistor, 2015. [Online]. Available: http://www.tandmresearch.com/

[16] TOKEN ELECTRONICS, Very Low Value Kelvin Four-Terminal Resistors, 2009. [Online]. Available: http://www.token.com.tw/

[17] K. Wang, X. Yang, H. Li, L. Wang, and P. Jain, "A high-bandwidth integrated current measurement for detecting switching current of fast GaN devices," *IEEE Trans. Power Electron.*, vol. 33, no. 7, pp. 6199–6210, Jul. 2018.

[18] TOKEN ELECTRONICS, "How 4-terminal resistor works," 2009. [Online]. Available: http://www.token.com.tw/
[19] M. Danilovic, Z. Chen, R. Wang, F. Luo, D. Boroyevich, and P. Mattavelli, "Evaluation of the switching characteristics of a gallium-nitride transistor," in *Proc. IEEE Energy Convers. Congr. Expo.*, 2011, pp. 2681–2688.
[20] D. Garrido, I. Baraia, J. Arza, and M. Barrenetxea, "Simple and affordable method for fast transient measurements of SiC devices," *IEEE Trans. Power Electron.*, vol. 35, no. 3, pp. 2933–2942, Mar. 2020.
[21] Ken Johnson and D. Maliniak, "Oscilloscope probes for power electronics: Be sure to choose the right probe for accurate measurements," *IEEE Power Electron. Mag.*, vol. 5, no. 1, pp. 37–44, Mar. 2018.
[22] Yuan Yang, Y. Wen, and Y. Gao, "A novel active gate driver for improving switching performance of high-power SiC MOSFET modules," *IEEE Trans. Power Electron.*, vol. 34, no. 8, pp. 7775–7787, Oct. 2018.
[23] Y. Shi, R. Xie, L. Wang, Y. Shi, and H. Li, "Switching characterization and short-circuit protection of 1200 V SiC MOSFET T-type module in PV inverter application," *IEEE Trans. Ind. Electron.*, vol. 64, no. 11, pp. 9135–9143, Mar. 2017.
[24] VISHAY, "Power metal strip resistors, very high power, low value, surface-mount," 30122 datasheet, Aug. 2018.
[25] K. Wang, L. Wang, X. Yang, X. Zeng, W. Chen, and H. A. Li, "Multiloop method for minimization of parasitic inductance in GaN-based high-frequency DC–DC converter," *IEEE Trans. Power Electron.*, vol. 32, no. 6, pp. 4728–4740, Jun. 2017.
[26] D. Reusch and J. Strydom, "Understanding the effect of PCB Layout on circuit performance in a high-frequency gallium-nitride-based point of load converter," *IEEE Trans. Power Electron.*, vol. 29, no. 4, pp. 2008–2015, Apr. 2014.
[27] T. Hashimoto, T. Kawashima, T. Uno, N. Akiyama, N. Matsuura, and H. Akagi, "A System-in-package (SiP) with mounted input capacitors for reduced parasitic inductances in a voltage regulator," *IEEE Trans. Power Electron.*, vol. 25, no. 3, pp. 731–740, Mar. 2010.
[28] T&M Research Products, Inc., Albuquerque, NM, USA, SDN-414-01, 2018. [Online]. Available: http://www.tandmresearch.com/
[29] CYBERTEK, CSD-01, 2019. [Online]. Available: http://www.cybertek.cn/
[30] Tektronix, Beaverton, OR, USA, TCP0200, 2019. [Online]. Available: https://www.tek.com.cn/
[31] PEM, CWT Mini & CWT MiniHF, 2013. [Online]. Available: http://www.pemuk.com/

Chengzi Yang (Student Member, IEEE) was born in 1993. He received the B.S. and M.S. degrees in electrical engineering from Shanghai University, Shanghai, China, in 2014 and 2017, respectively. He is currently working toward the Ph.D. degree in electrical engineering with Xi'an Jiaotong University, Xi'an, China.

His research interests include gate drive technologies of wide-bandgap semiconductors and design of high-power high-voltage power converters.

Yunqing Pei (Member, IEEE) was born in 1969. He received the B.S. and M.S. degrees both in electrical engineering and the Ph.D. degree in power electronics from Xi'an Jiaotong University, Xi'an, China, in 1991, 1994, and 1999, respectively.

He became a Faculty Member of Xi'an Jiaotong University, where he is currently a Professor. From February 2006 to February 2007, he was a Visiting Scholar with the Center of Power Electronics Systems, Virginia Polytechnic Institute and State University. His research interests include the high-power inverters, switch-mode power supply, and converters in distributed generation systems.

Laili Wang (Senior Member, IEEE) received the B.S., M.S., and Ph.D. degrees from the School of Electrical Engineering, Xi'an Jiaotong University, Xi'an, China, in 2004, 2007, and 2011, respectively.

Since 2011, he has been a Postdoctoral Research Fellow with the Electrical Engineering Department, Queen's University, Kingston, ON, Canada. From 2014 to 2017, he was an Electrical Engineer with Sumida, Kingston, ON, Canada. In 2017, he joined Xi'an Jiaotong University, as a Full Professor. His research interests include package and integration, wireless power transfer, and energy harvesting.

Dr. Wang serves as an Associate Editor of IEEE TRANSACTIONS ON POWER ELECTRONICS and IEEE JOURNAL OF EMERGING AND SELECTED TOPICS IN POWER ELECTRONICS. He is the Vice Chair of Technical committee of Power Conversion Systems and Components in PELS, Co-Chair of System Integration and Application in International Technology Roadmap for Wide Band-gap Power Semiconductor, and Chair of IEEE CPSS and PELS Joint Chapter in Xi'an, China.

Longyang Yu (Student Member, IEEE) was born in 1992. He received the B.S. degree in electrical engineering from the Xi'an University of Technology, Shaanxi, China, in 2015. He is currently working toward the Ph.D. degree in electrical engineering with Xi'an Jiaotong University, Xi'an, China.

His research interests include power electronic topology, applications of power semiconductor devices, and magnetic component integration based on wide bandgap power semiconductor devices.

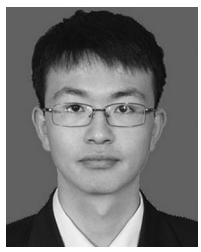

Cheng Zhao (Student Member, IEEE) was born in Shanxi, China, in 1996. He received the B.S. degree in electrical engineering from Jilin University, Changchun, China, in 2017. He is currently working toward the Ph.D. degree in electronic and electrical engineering with Xi'an Jiaotong University, Xi'an, China.

His research interests include packaging and applications of wide bandgap power semiconductor devices and parallel operation of SiC MOSFETs.

Mengyu Zhu was born in 1997. She received the B.S. degree in electrical engineering and automation from China University of Mining and Technology, Xuzhou, China, in 2018. She is currently working toward the M.S. degree in electrical engineering with Xi'an Jiaotong University, Xi'an, China.

Her research interests include gate drive technologies of wide-bandgap semiconductors and design of high-power high-voltage power converters.

Xingshuo Liu was born in 1997. He received the B.S. degree in electrical engineering and automation from Wenhua College, Wuhan, China, in 2019. He is currently working toward the M.S. degree in electrical engineering with Xi'an Jiaotong University, Xi'an, China.

His research interests include gate drive technologies of wide-bandgap semiconductors and design of high-power high-voltage power converters.